



Formation mechanism of nanosecond-laser-induced microstructures on amorphous silicon film surfaces

YINGMING REN^{1,2} AND ZHIYU ZHANG^{1,*}

¹Key Laboratory of Optical System Advanced Manufacturing Technology, Changchun Institute of Optics, Fine Mechanics and Physics, Chinese Academy of Sciences, Changchun, Jilin 130033, China

²University of Chinese Academy of Sciences, Beijing 100049, China

*zhangzhiyu@ciomp.ac.cn

Abstract: Laser-induced microstructures have attracted significant research interest owing to their wide application potential for anti-reflective surfaces and optoelectronic devices. To elucidate the characteristics of laser-patterned microstructures, nanosecond-laser-induced micro-protrusions on amorphous silicon film surfaces were investigated via single- and multi-line irradiation experiments. For the former, the results reveal that the number of periodic micro-protrusions depends on the peak power intensity. In addition, the height and the base diameter of the micro-protrusions can be tailored by adjusting the peak power intensity and scanning distance of the laser, while increasing the peak power intensity also increases surface roughness. X-ray spectroscopy confirmed that the microstructures were mainly composed of silicon. The relationship between the formation mechanism and the size of the micro-protrusions is also discussed, with the results of this study providing valuable insights into the laser-induced microstructure formation.

© 2021 Optical Society of America under the terms of the [OSA Open Access Publishing Agreement](#)

1. Introduction

The preparation of micro/nanostructures is relevant for multiple applications involving structures such as photonic crystals, metamaterials, and superhydrophobic/hydrophilic surfaces [1–3]. Laser processing has been studied extensively as a technique for fabricating microstructures on various materials [4–8]. For example, Gedvilas et al. [9] manufactured a highly periodic array of dimples on the silicon surface through laser interference patterning technology. Previous studies have identified several mechanisms thought to play a decisive role in the formation of micro/nanostructures [10–13]. Of these mechanisms, the interference between incident and scattered light has gained widespread acceptance.

In general, the periodicity of micro/nanostructures is close to the wavelength of the incident laser light, particularly when using lasers with a longer pulse duration. For example, Zhou et al. [12] produced spontaneous periodic surface structures whose periodicity approximately matched the laser wavelength on metal surfaces using picosecond laser irradiation. Moreover, Bonch-Bruевич et al. [11] reported the formation of periodic structures with a periodicity ranging from 0.5–1 times the laser wavelength using polarized irradiation at large incident angles with millisecond pulse durations.

However, our recent studies have shown that the periodicity of nanosecond-laser-induced microstructures can differ notably from the laser wavelength under certain conditions, resulting in structures with a periodicity that is more than 50 times that of the laser wavelength. More interestingly, it was demonstrated that both the number and dimensions of the columns comprising the microstructures can be controlled using the peak power intensity of single-line laser irradiation. Nevertheless, further research is required to obtain a comprehensive understanding of the mechanisms governing the formation of nanosecond-laser-induced microstructures.

In this study, we realized novel periodic micro-protrusions on the surface of an amorphous silicon film using nanosecond-laser irradiation. The effect of the peak power intensity and scanning distance on nanosecond-laser-induced microstructures was investigated using a combination of single-line and multi-line irradiation methods. The shape, basement diameter, height, and material composition of the microstructures were investigated under various conditions. The dependences of the microstructure height on the laser peak power intensity and scanning distance were obtained. In addition, the mechanisms underlying the formation of microstructures with different sizes are discussed in the context of micro/nanostructure applications.

2. Materials and methods

2.1. Materials

Typically, amorphous silicon films are deposited on metal or ceramic substrates using glow discharge chemical vapor deposition, vacuum magnetron sputtering deposition, or plasma-enhanced processes [14]. These approaches can produce amorphous silicon films measuring several hundreds of square centimeters. In this experiment, a polished reaction-bonded silicon carbide (RB-SiC) substrate was coated with an amorphous silicon film with a thickness of 22 μm using a vacuum magnetron sputtering deposition process, and the surface roughness of the RB-SiC substrate was 3 nm in Ra. Initially, the surface roughness of the silicon film was characterized by features with an average size of 12 nm, as determined by confocal laser scanning microscopy (CLSM).

2.2. Experimental procedures

The amorphous silicon films were irradiated using a nanosecond-pulse laser machining system with a wavelength of 532 nm (EP30-G8, Changchun New Industries Optoelectronics Technology Co., Ltd., China). The system employs a galvanometer mirror to achieve two-dimensional scanning in air. The beam has a Gaussian energy density distribution and the telecentric f-theta objective lens with the focal length of 160 mm was used to focus the beam on the surface of the target material. The real spot size is 80 μm , evaluated using the diameter squared versus fluence method [15]. During the microstructure fabrication experiments, the pulse width was maintained at 46 ns. For multi-line irradiation, the distance between the two scanning lines varied from 30–80 μm , corresponding to beam overlap ratios ranging from 87.5–37.5%. To ensure pulse overlap, the laser scanning speed was set to 50 mm/s. Average laser powers of 6–20 W were used, corresponding to peak laser powers ranging from $0.935\text{--}3.12 \times 10^6$ W. The average laser power

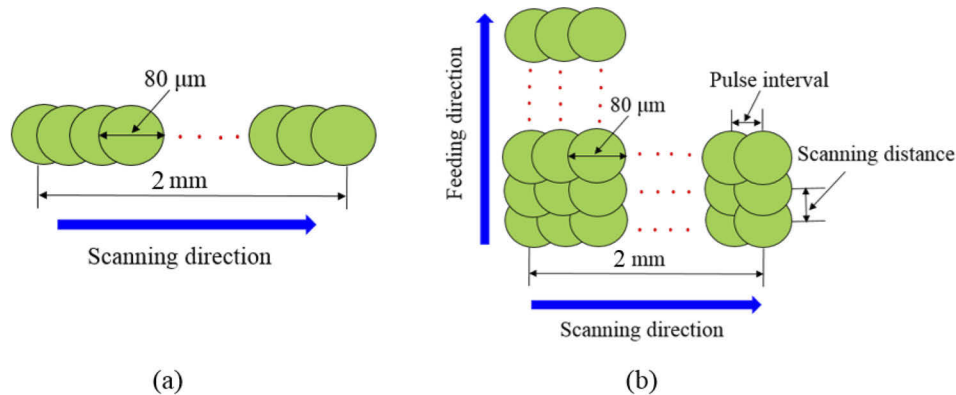


Fig. 1. Diagrams of the laser scanning path for (a) single-line and (b) multi-line irradiation.

is the average value of ten times measured using power meter. Its standard deviation is 1.8–2.0%. According to Guo and Caslaru [16], the peak power intensities were calculated to be within the range of $0.465\text{--}1.55 \times 10^{10} \text{ W/cm}^2$.

Figure 1 shows the laser scanning path. For single-line irradiation, line scanning was performed from left to right, with the line having an overall length of 2 mm [Fig. 1(a)]. For multi-line irradiation, after completing an initial irradiation process, the laser beam was shifted along the feeding direction according to the selected scanning distance, resulting in an overlap between the two scanning lines [Fig. 1(b)]. The laser irradiation conditions are summarized in Table 1. Following the laser irradiation operation, the surface topography of the samples was measured using CLSM (OLYMPUS, OLS4100) and scanning electron microscope (FE-SEM, HITACHI S4800). Subsequently, the elemental compositions of the unirradiated and irradiated regions were compared using energy-dispersive X-ray spectroscopy (EDX; EDAX Genesis).

Table 1. Laser irradiation conditions.

Parameter name	Parameter setting
Laser type	Nanosecond pulsed laser
Wavelength	532 nm
Pulse width	46 ns
Scanning distance	30–80 μm
Irradiation region	2 mm \times 2 mm
Peak power intensity	$4.65 \times 10^9\text{--}1.55 \times 10^{10} \text{ W/cm}^2$
Specimen	Amorphous silicon film
Environment	In air

3. Results and discussion

3.1. Single-line irradiation

Figure 2 shows optical images of the surface morphologies of laser-irradiated regions corresponding to different peak power intensities with a repetition frequency of 140 kHz [17]. As shown in Fig. 2(a), for single-line irradiation at a peak power intensity of $4.65 \times 10^9 \text{ W/cm}^2$, a row of micro-protrusions was formed on the silicon film surface with their location corresponding to the center of the beam. Figure 2(b) shows the morphology created using a higher peak power intensity of $6.02 \times 10^9 \text{ W/cm}^2$: multiple rows of laser-induced micro-protrusions were formed, exhibiting a periodic distribution. Upon inspection of the image, it is evident that the micro-protrusions are parallel to the scanning direction of the sample. Increasing the peak power intensity to $7.31 \times 10^9 \text{ W/cm}^2$ resulted in an increase in the number of rows of micro-protrusions increasing (in odd rows), and in the appearance of micro-cracks on the surface owing to the effects of thermal stress and thermal expansion [Fig. 2(c)]. As shown in Fig. 2(d), in response to increasing the laser peak power intensity still further, the surface of the silicon film was partially ablated because the laser energy exceeded the ablation threshold of silicon. This is confirmed by the SEM image in Fig. 2(g). Increasing the laser peak power intensity further causes the ablation region to increase in size. As shown in Fig. 2(f), the laser-irradiated zone eventually becomes a micro-groove comprising a hybrid micro/nanostructure. As shown by the graph in Fig. 2(f), silicon atoms at the edge of the micro-groove are ejected in an anisotropic manner from the micro-groove under high laser peak power intensities. In addition, as shown in Figs. 2(g)–(i), as the laser peak power intensity increases, additional surface material is ablated and re-deposited on the surface to form a thicker recast layer.

To evaluate the influence of these micro-protrusions on the formation of the structure, CLSM was used to examine their morphological properties. Figure 3 shows the micro-protrusion

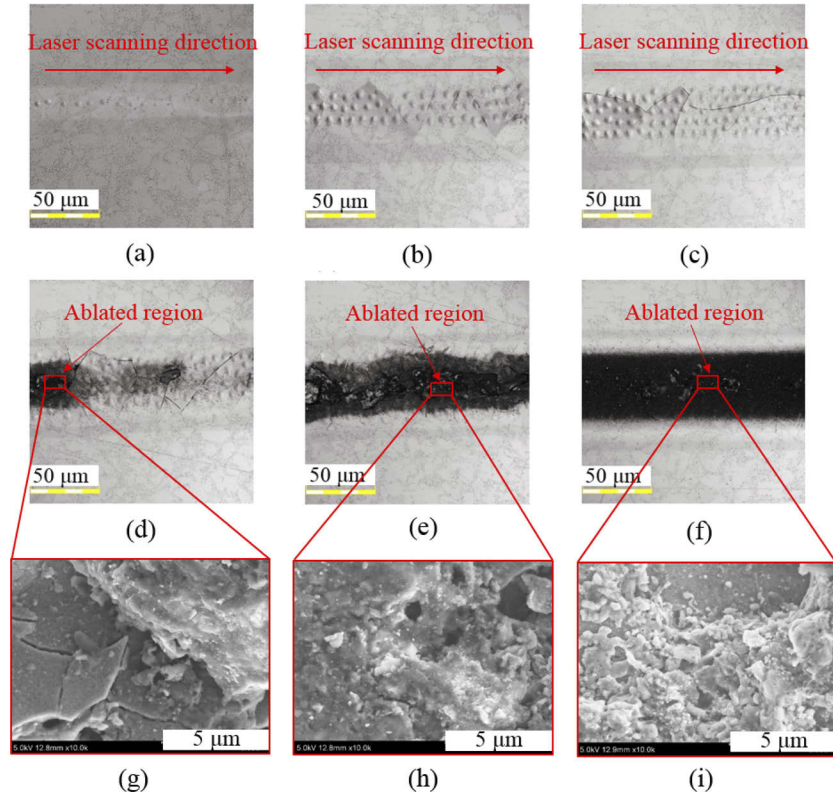


Fig. 2. Surface morphologies of single-line irradiated regions using a laser with a pulse width of 46 ns at different peak power intensities; (a) 4.65×10^9 W/cm², (b) 6.02×10^9 W/cm², (c) 7.31×10^9 W/cm², (d) 8.54×10^9 W/cm², (e) 9.85×10^9 W/cm², (f) 1.21×10^{10} W/cm², (g) SEM image of the ablated region in (d), (h) SEM image of the ablated region in (e), (i) SEM image of the ablated region in (f).

periodicities corresponding to several different laser power peak intensities. The average micro-protrusion periodicity was measured as 30 ± 0.05 μm. This result suggests that the micro-protrusion is largely unaffected by increasing the peak power intensity. According to previous studies [12], the periodicity of the laser-induced surface structure (D) is closely related to the wavelength, as expressed by

$$D = \frac{\lambda}{1 \pm \sin \theta}, \quad (1)$$

where λ is the laser wavelength and θ is the angle of incidence measured from the normal to the surface. However, Figs. 2(a)–(d) clearly show that the distance between the micro-protrusions is substantially different from the wavelength.

3.2. Multi-line irradiation

3.2.1. Effect of scanning distance

As shown in Figs. 2(b)–(d), increasing the peak power intensity allows for the formation of multiple rows of micro-protrusions, although the spacing between each row remains at an approximately constant value of 30 μm. To manufacture micro-protrusions with different pitches, we irradiated the silicon film surface using a laser peak power intensity of 4.65×10^9 W/cm² based on the morphology shown in Fig. 2(a). Figure 4 shows the three-dimensional surface topographies

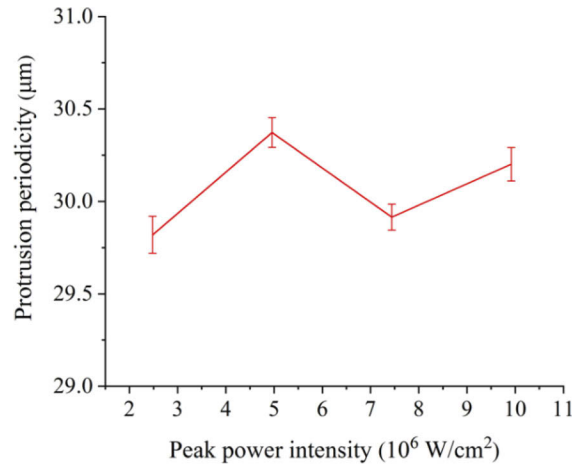


Fig. 3. Micro-protrusion periodicity at different laser peak power intensities.

achieved by changing the scanning distance while maintaining the repetition frequency at 140 kHz. At scanning distances of 80 μm and 70 μm , microcracks appear on the irradiated silicon film surfaces, affecting the formation of micro-protrusions [Figs. 4(a) and (b)]. As the scanning distance decreases, the microcracks gradually disappear owing to the larger melting volume caused by the laser irradiation. Notably, there are almost no microcracks on the surface when the scanning pitch is 40 μm .

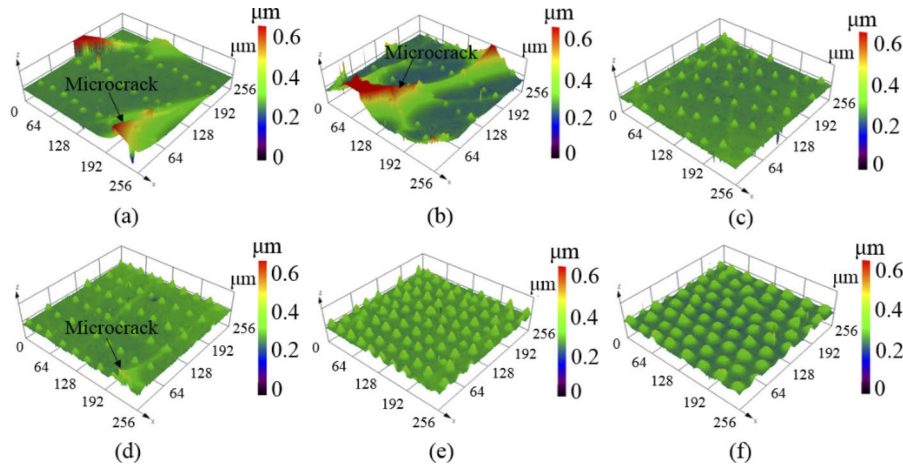


Fig. 4. Three-dimensional surface topographies of silicon film surfaces irradiated at different scanning distances with a peak power intensity of $4.65 \times 10^9 \text{ W/cm}^2$ and a repetition frequency of 140 kHz; (a) 80 μm , (b) 70 μm , (c) 60 μm , (d) 50 μm , (e) 40 μm , (f) 30 μm .

Another consequence of decreasing the scanning distance is that the base diameter and height of the micro-protrusions both increase, as shown in Figs. 5 and 6. Specifically, the average base diameter increased from 11.201 μm to 24.750 μm , while the average height increased from 0.142 μm to 0.315 μm . The increase in the melting area promotes micro-protrusion growth. The average base diameter and height of the micro-protrusions are average value of ten times measured using CLSM. The standard deviation of the base diameter and height is 7.7–8.9% and

1.7–1.9%, respectively. In addition, it should be noted that the basement diameter and height of the micro-protrusions can be tuned by changing the laser scanning distance, allowing for the creation of various effective surface regions; this is referred to as the beam-overlap effect.

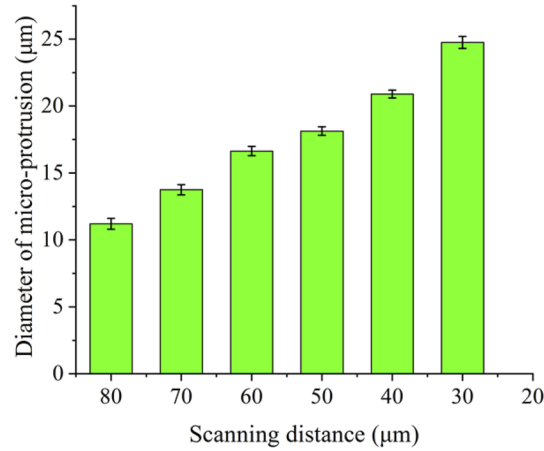


Fig. 5. Average base diameter of the micro-protrusions at various scanning distances.

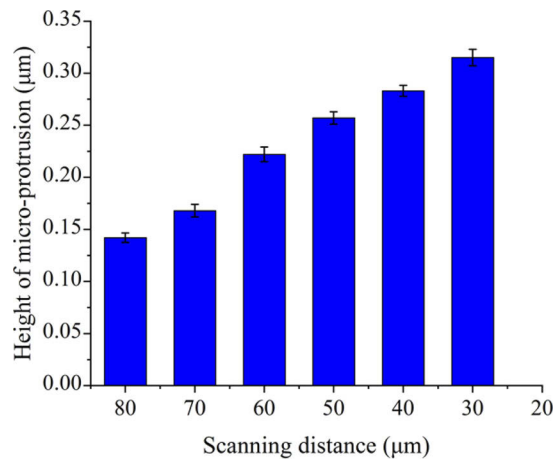


Fig. 6. Average height of the micro-protrusions at various scanning distances.

The surface roughness of the amorphous silicon films changes with the scanning distance changes irrespective of the peak power intensity of the laser. Figure 7 shows a plot of surface roughness as a function of beam scanning distance under a peak power intensity of 4.65×10^9 W/cm². For a scanning distance of 80 μm, the surface roughness is more pronounced than the initial surface. In general, microcracks are generated in the subsurface during grinding [18]. Such internal microcracks are relatively difficult to detect from the surface. During laser irradiation at a large scanning distance, the thermal expansion resulting from the increase in temperature causes these internal microcracks to open up rather than melt the surface layer. In their opened state, the microcracks manifest as an increase in surface roughness. By decreasing the scanning distance to induce melting, the surface roughness decreases owing to the reduction in the number of microcracks. However, at scanning distances below 60 μm, the surface roughness becomes

more prominent again. In this case, the increased surface roughness can be attributed to the increase in the base diameter and height of the micro-protrusions.

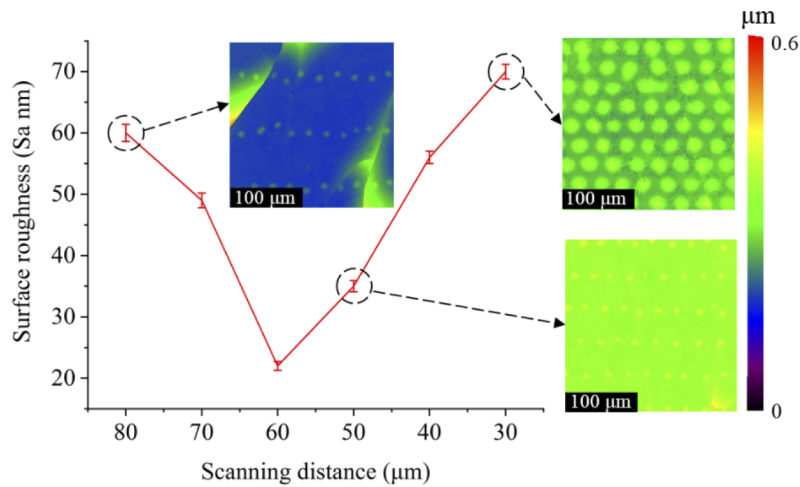


Fig. 7. Measured surface roughness of the irradiated region at various scanning distances.

3.2.2. Effect of peak power intensity

Figure 4 shows that relatively uniform micro-protrusions were obtained when using a scanning distance of 40 μm was applied. Multi-line irradiation at different peak power intensities was conducted to elucidate the effect of peak power intensity on micro-protrusion formation. Figure 8 shows two- and three-dimensional surface topographies at three different laser peak power intensities, with the repetition frequency set to 140 kHz and a scanning distance of 40 μm. For a peak power intensity of 4.65×10^9 W/cm², it should be noted that the micro-protrusions on the surface of the silicon film are grouped together, resulting in mound-like formations with a certain periodicity that are repeated along the laser beam sweeping line [Fig. 8(a)]. The average micro-protrusion base diameter was measured as 22.36 μm, while the average height was measured as 0.28 μm.

Increasing the peak power intensity of the laser irradiation to 1.21×10^{10} W/cm² resulted in the formation of multiple disordered micro-dot structures, as shown in Fig. 8(b). Particle production was also observed. These particles are scattered by the laser irradiation process and reattach to the material surface during recrystallization. Therefore, at larger laser energies, part of the irradiated material is ejected. As time progresses, the vaporized material cools and is deposited and re-solidified on the surface of the irradiated areas [19]. By increasing the laser peak power intensity further to 1.55×10^{10} W/cm², taller and broader microstructures were generated, as shown in Fig. 8(c). However, the morphology of these microstructures was conspicuously different, with the shape changing from micro-protrusions to comb-like structures. Approximately 80% of the structures were taller than 16 μm, with the average basement diameter of the structures increasing to 26.87 μm.

3.3. Energy-dispersive X-ray spectroscopy analysis

We used EDX to analyze the elemental composition of the irradiated sample regions, with the results shown in Fig. 9. Unsurprisingly, prior to laser irradiation, the outer layer of the amorphous silicon film was comprised overwhelmingly of Si, with traces of C and O [Fig. 9(a)]. As shown in Figs. 9(b)–(d), the irradiated surfaces contain relatively more O content (increased from 3.51%

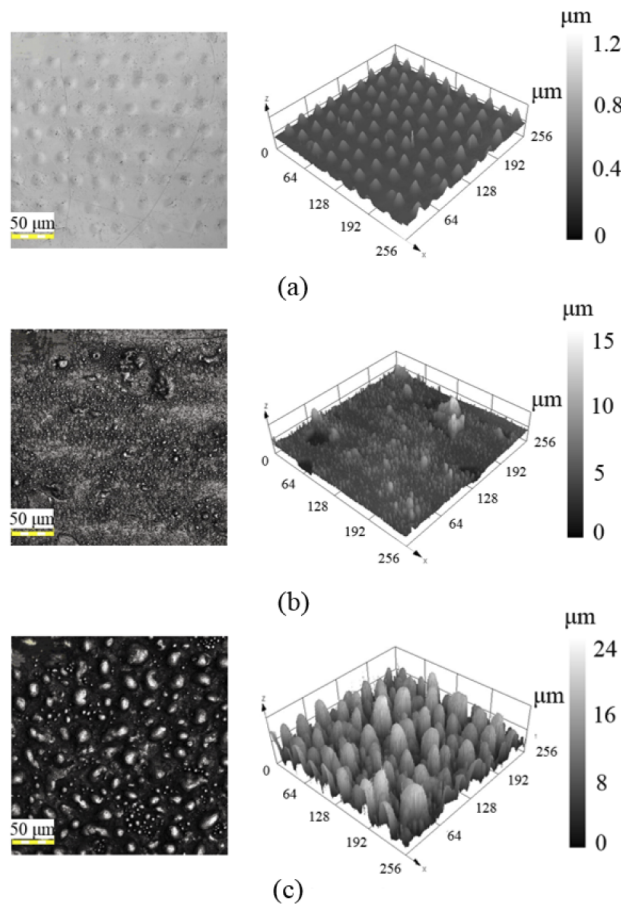


Fig. 8. Two- and three-dimensional profiles of silicon film surfaces processed by laser irradiation at different laser peak power intensities with a scanning distance of 40 μm ; (a) $4.65 \times 10^9 \text{ W/cm}^2$, (b) $1.21 \times 10^{10} \text{ W/cm}^2$, (c) $1.55 \times 10^{10} \text{ W/cm}^2$.

to 16.42%), indicating that the surface of the microstructures becomes increasingly oxidized as the peak power intensity of the laser increases. Nevertheless, Si remains the principal component of the microstructures. Consequently, it can be inferred that, for microstructural formation at a low peak power intensity, micro-protrusions are formed via the re-solidification of molten material, while, at a high peak power intensity, the plasma recoil pressure promotes the formation of comb-like structures.

3.4. Micro-protrusion formation mechanism

The mechanism of microstructure formation on the surface of the silicon films is rather complex. Many analyses [20–22] have shown that the major parameters affecting microstructural characteristics such as physical dimensions and periodicity may include the initial surface conditions, the thickness of the thin film, the internal material ultrastructure (e.g., single-crystalline, polycrystalline, or amorphous), the hydrodynamics involved in the evaporation/melting of the surface layer, and the laser irradiation parameters (e.g., pulse width, laser wavelength, ambient temperature, type of gaseous medium, peak power intensity, and repetition frequency).

To understand the process of laser heat transfer and explore the microstructure formation mechanism, the evolution of surface temperature during the pulsed laser irradiation was simulated

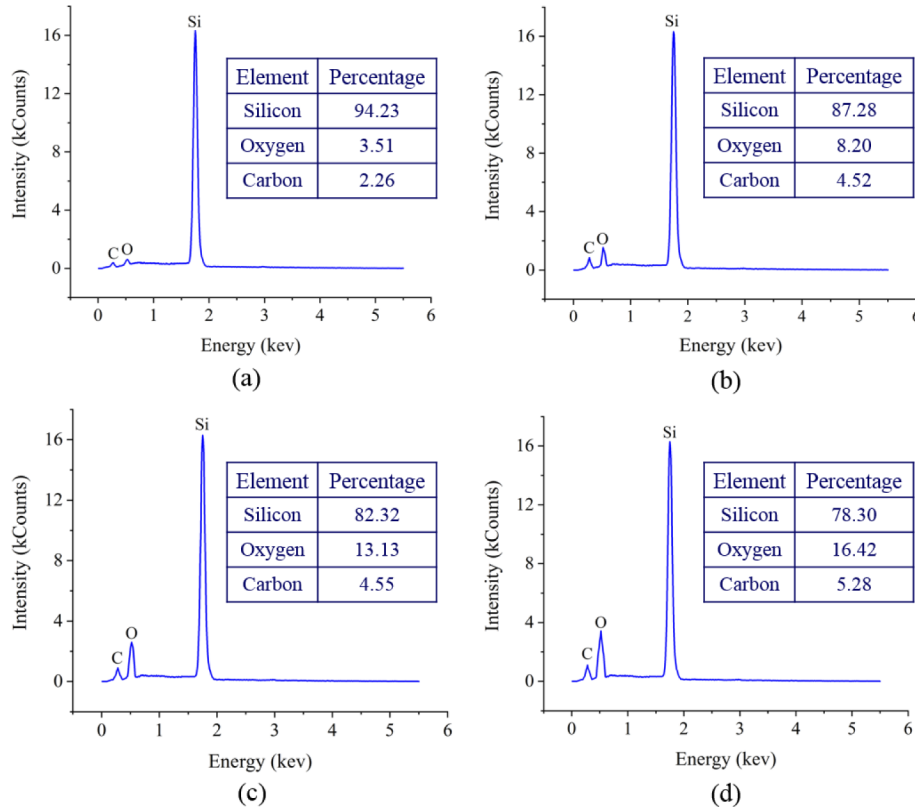


Fig. 9. Energy-dispersive X-Ray spectroscopy results for micro-structures fabricated using different laser peak power intensities; (a) Original surface, (b) $4.65 \times 10^9 \text{ W/cm}^2$, (c) $1.21 \times 10^{10} \text{ W/cm}^2$, (d) $1.55 \times 10^{10} \text{ W/cm}^2$.

using the thermal model proposed in Ref. [23–25]. The simulation calculations were performed using COMSOL Multiphysics software. Heat transfer happens via heat conduction to the material interior, and heat dissipation via natural convection and irradiation at the material interface. Meantime, evaporation of materials can also bring about energy loss. The process of heat transfer can be expressed as follows:

$$\rho C_p \frac{\partial T}{\partial t} = \nabla \cdot (k \nabla T) + Q, \quad (2)$$

where ρ is the density, C_p is the specific heat capacity of the material under constant pressure, T is the temperature, k is the thermal conductivity, and Q is the incident heat source, which can be expressed as follows:

$$Q(x, y, z, t) = R \frac{4\pi h_k}{\lambda} \cdot \frac{P}{\pi r_0^2} \exp\left(-\frac{2(x^2 + y^2)}{r_0^2}\right) \exp\left(-z \frac{4\pi h_k}{\lambda}\right), \quad (3)$$

where h_k is the imaginary part of the refractive index, λ is the laser wavelength, R is the absorptivity of the laser energy, P is the incident laser average power, and r_0 is the beam radius at $1/e^2$ of a Gaussian laser profile.

Figure 10 shows the results corresponding to laser peak power intensities of $4.65 \times 10^9 \text{ W/cm}^2$, $6.02 \times 10^9 \text{ W/cm}^2$, and $7.31 \times 10^9 \text{ W/cm}^2$, where the melting temperature is 1688 K. Note that the peak temperature exceeds the melting point but remains lower than the boiling point (2629 K) at each of these three peak power intensities, with the surface temperature falling below the

melting point extremely quickly (14 μs) after the irradiation pulse. For peak power intensities of $1.21 \times 10^{10} \text{ W/cm}^2$ and $1.55 \times 10^{10} \text{ W/cm}^2$, the peak surface temperature rises above the boiling point, as shown in Fig. 11. In these cases, some material from the center of the irradiated area evaporates as extremely fine vapor particles as opposed to explosive boiling.

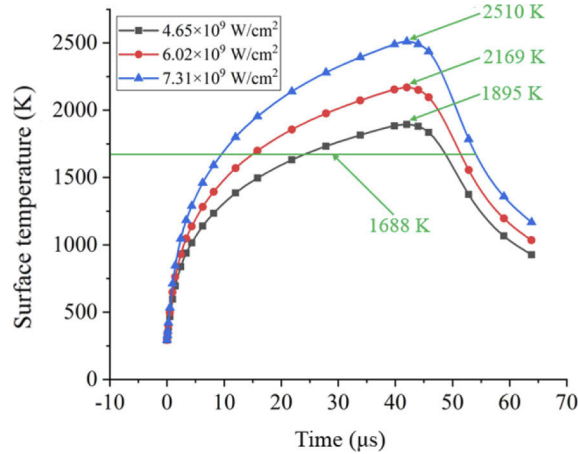


Fig. 10. Calculated surface temperature as a function of time for irradiation with different laser peak power intensities.

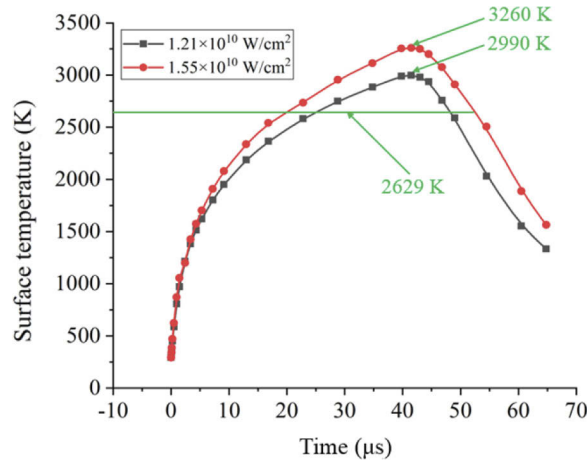


Fig. 11. Calculated surface temperature as a function of time for irradiation with different laser peak power intensities.

Figure 12 presents a schematic of the possible mechanism underlying the laser-induced formation of micro-protrusions on amorphous silicon films. It is known that laser irradiation can cause thermal accumulation on the surface of the material to the extent that melting or ablation occur [26,27]. At a low peak power intensity of $4.65 \times 10^9 \text{ W/cm}^2$, the silicon film is directly heated and melted via laser irradiation. However, as shown in Fig. 12(b₁), owing to the temperature gradient associated with the Gaussian energy distribution, the maximum melting depth at the center of the beam and the melt pool is small [28–30]. In contrast, as shown in Fig. 12(b₂) and (b₃), a larger heat-affected zone forms beneath the liquidized materials as well as on the upper surface as the peak power intensity increases. Because of the low peak intensity, any

plasma shielding effect is negligible, resulting in weak or no plasma formation [31]. However, the solid/liquid interface protuberates in the central zone because of the fluctuations created via the continuous pulse shocks at a repetition frequency of 140 kHz. The temperature gradient in the area around the protrusion increases, thereby promoting the growth of the protrusion. While the protrusion becomes more pronounced, surface tension owing to the Gibbs-Thomson effect makes the protrusion an arc shape [32]. As shown in Fig. 10, under a high cooling rate, a number of small micro-protrusions remain on the top surface, with the number of columnar micro-protrusions increasing as the size of the molten area increases [Fig. 12(c₁–c₃)].

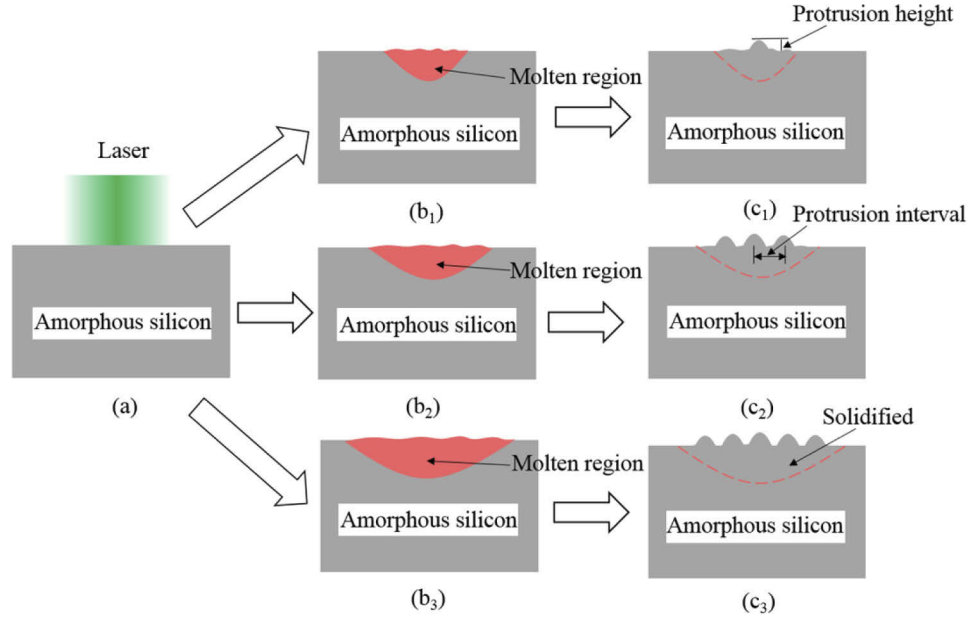


Fig. 12. Schematic showing the micro-protrusion formation mechanism for various laser peak power intensities; (a) Laser irradiated surface, (b₁) The molten pool under peak power intensity of $4.65 \times 10^9 \text{ W/cm}^2$, (b₂) The molten pool under peak power intensity of $6.02 \times 10^9 \text{ W/cm}^2$, (b₃) The molten pool under peak power intensity of $7.31 \times 10^9 \text{ W/cm}^2$, (c₁) Single row of micro-protrusions, (c₂) Three rows of micro-protrusions, (c₃) Five rows of micro-protrusions.

Figure 13 presents a schematic of the possible mechanism underlying the formation of comb-like microstructures on irradiated amorphous silicon films. At high peak power intensities, maximum surface temperatures of 2990 K and 3260 K were recorded during laser irradiation, both of which exceed the boiling point of amorphous silicon (2629 K), as shown in Fig. 11. For a peak power intensity of $1.21 \times 10^{10} \text{ W/cm}^2$, the laser irradiation causes the silicon to vaporize, resulting in splatter on the surface. Thus, vaporized silicon can be redeposited on the film surface [33]. Moreover, the accumulation of material particulates results in the formation of a recast layer. Weak plasma formation was observed under these conditions. Because the plasma pressure is not sufficient to promote molten silicon to a significant height above the original surface, the silicon protrusions manifest as small bump-shaped structures, as shown in Fig. 8(b).

As shown in Fig. 8(c), when the peak power intensity increases to $1.55 \times 10^{10} \text{ W/cm}^2$, sufficient material is vaporized to generate a powerful plasma, and the high peak power intensity elevates the recoil pressure, which may force the molten material to move upward at high speed [34]. In addition, at a high peak power intensity, a higher temperature can be maintained for longer, which preserves the material in a molten state and facilitates the transport of molten material on the

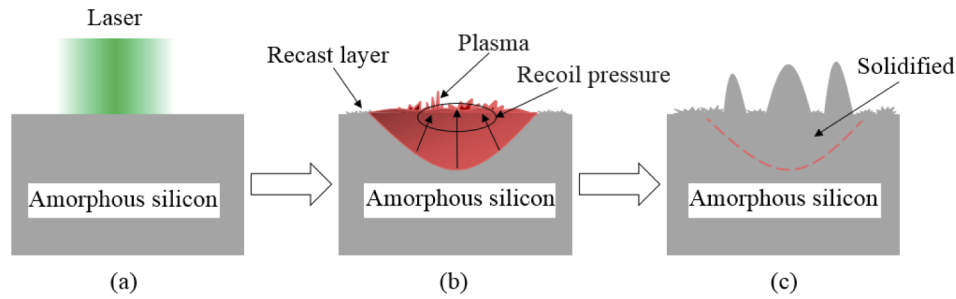


Fig. 13. Schematic showing the mechanism underlying the formation of comb-like protrusions under a peak power intensity of $1.55 \times 10^{10} \text{ W/cm}^2$; (a) Laser irradiated surface, (b) Laser-induced plasma, (c) Comb-like protrusions.

original surface [35]. Thus, the more substantial melt pool volume and recoil pressure generated by the laser-induced plasma can promote molten material comfortably above the original surface, where it cools rapidly to form comb-like protrusions on the top surface, as shown in Fig. 13. The resultant protrusions have large base diameters and heights.

4. Conclusions

In this study, microstructures of different heights were fabricated on silicon film surfaces using nanosecond-laser irradiation (wavelength: 532 nm) with various peak power intensities. The following conclusions can be drawn from our experiments and analysis:

1. During single-line irradiation, the number of micro-protrusions increases in odd-numbered increments in response to increasing the peak power intensity. The micro-protrusions have an average periodicity of $30 \pm 0.05 \mu\text{m}$. When the peak power intensity exceeds $8.54 \times 10^9 \text{ W/cm}^2$, the micro-protrusions disappear, resulting in ablation of the film surface.
2. Under a peak power intensity of $4.65 \times 10^9 \text{ W/cm}^2$, the periodicity of the micro-protrusions perpendicular to the scanning direction can be tuned by controlling the laser scanning distance. Under this condition, uniform micro-protrusions can be manufactured over a large area.
3. The surface roughness, base diameter, and height of the micro-protrusions is increased by decreasing the scanning distance, which has the added effect of introducing microcracks that contribute to the surface roughness.
4. The formation of the micro-protrusions is attributed to fluctuations created by continuous pulse shocks at a high repetition frequency, which promotes the growth of protuberances at the solid/liquid interface at the center of the beam.
5. Increasing the peak power intensity to $1.55 \times 10^{10} \text{ W/cm}^2$ leads to the formation of a comb-like protrusion on the silicon film surface, which is due to the strong laser-induced plasma recoil pressure forcing molten material upwards to a height substantially above the original surface.

In summary, the results demonstrate that microstructures of various heights can be fabricated on amorphous silicon film surfaces under different peak power intensities. Our results offer crucial insights into the formation mechanism and periodicity of laser-induced microstructures, which is significant because lasers are a popular method for patterning materials used in applications such as superhydrophobic/hydrophilic surfaces and flexible solar panels.

Funding. Chinese Academy of Sciences Key Project (QYZDJ-SSW-JSC038); Department of Science and Technology of Jilin Province (20180520202JH); Bureau of International Cooperation, Chinese Academy of Sciences (181722KYSB20180015); National Natural Science Foundation of China (51775531, 11803037).

Disclosures. The authors declare no conflicts of interest.

Data availability. Data underlying the results presented in this paper are not publicly available at this time but may be obtained from the authors upon reasonable request.

References

1. L. He, J. Xu, Z. Dekai, Q. H. Yang, and L. Q. Li, "Potential application of functional micro-Nano structures in petroleum," *Petroleum Exploration and Development* **45**(4), 745–753 (2018).
2. N. Sharma, M. Hooda, and S. K. Sharma, "Fabrication of micro-nano-mechanical structures for sensing application," *Int. J. Appl. Eng. Res.* **13**(8), 6388–6393 (2018).
3. F. Chen, J. Du, and S. Huang, "Fabrication of repairable anti-corrosive superhydrophobic surfaces with micro-Nano structures by ultrasonic cavitation," *Appl. Surf. Sci.* **541**(10), 148605 (2020).
4. X. Yang, J. Liu, X. Cui, G. Jin, Z. Liu, Y. Chen, and X. Feng, "Effect of remelting on microstructure and magnetic properties of Fe-Co-based alloys produced by laser additive manufacturing," *J. Phys. Chem. Solids* **130**, 210–216 (2019).
5. F. Madani-Grasset and Y. Bellouard, "Femtosecond laser micromachining of fused silica molds," *Opt. Express* **18**(21), 21826–21840 (2010).
6. I. W. Boyd, *Laser processing of thin films and microstructures*, (Springer, 1987), p. 148.
7. T. E. Abioye, P. K. Farayibi, P. Kinnel, and A. T. Clare, "Functionally graded Ni-Ti microstructures synthesised in process by direct laser metal deposition," *Int J Adv Manuf Technol* **79**(5-8), 843–850 (2015).
8. Y. B. Gao, B. X. Wu, Y. Zhou, and S. Tao, "A two-step nanosecond laser surface texturing process with smooth surface finish," *Appl. Surf. Sci.* **257**(23), 9960–9967 (2011).
9. M. Gedvilas, S. Indrišiūnas, B. Voisiat, E. Stankevičius, A. Selskis, and G. Račiukaitis, "Nanoscale thermal diffusion during the laser interference ablation by femto-, pico-, and nanosecond pulses in silico," *Phys. Chem. Chem. Phys.* **20**(17), 12166–12174 (2018).
10. J. E. Sipe, "Laser-induced periodic surface structure. I. Theory," *Phys. Rev. B* **27**(2), 1141–1154 (1983).
11. A. M. Bonch-Bruевич, M. N. Libenson, and V. S. Makin, "Surface electromagnetic waves in optics," *Opt. Eng.* **31**(4), 718–730 (1992).
12. G. S. Zhou, P. M. Fauchet, and A. E. Siegman, "Growth of spontaneous periodic surface structures on solids during laser illumination," *Phys. Rev. B* **26**(10), 5366–5381 (1982).
13. H. Huang and J. W. Yan, "Surface patterning of Zr-based metallic glass by laser irradiation induced selective thermoplastic extrusion in nitrogen gas," *J. Micromech. Microeng.* **27**(7), 075007 (2017).
14. R. Bock, J. Schmidt, and R. Brendel, "Effective passivation of highly aluminum-doped p-type silicon surfaces using amorphous silicon," *Appl. Phys. Lett.* **91**(11), 112112 (2007).
15. A. Žemaitis, M. Gaidys, M. Brikas, P. Gečys, G. Račiukaitis, and M. Gedvilas, "Advanced laser scanning for highly-efficient ablation and ultrafast surface structuring: experiment and model," *Sci. Rep.* **8**(1), 17376 (2018).
16. Y. B. Guo and R. Caslaru, "Fabrication and characterization of micro dent arrays produced by laser shock peening on titanium Ti–6Al–4 V surfaces," *J. Mater. Process. Technol.* **211**(4), 729–736 (2011).
17. Y. M. Ren and Z. Z. Zhang, "Influences of Initial Surface Conditions on Response Characteristics of Amorphous Silicon Films to Nanosecond Laser Irradiation," *Micromachines* **12**(7), 807 (2021).
18. K. Niitsu and J. W. Yan, "Effects of deep subsurface damages on surface nanostructure formation in laser recovery of grinded single-crystal silicon wafers," *Precis. Eng.* **62**, 213–222 (2020).
19. H. Huang, N. Jun, M. Jiang, M. Ryoko, and J. Yan, "Nanosecond pulsed laser irradiation induced hierarchical micro/nanostructures on Zr-based metallic glass substrate," *Mater. Des.* **109**, 153–161 (2016).
20. T. Tavera, N. Pérez, A. Rodríguez, P. Yurrita, S. M. Olairola, and E. Castaño, "Periodic patterning of silicon by direct nanosecond laser interference ablation," *Appl. Surf. Sci.* **258**(3), 1175–1180 (2011).
21. V. V. Iyengar, B. K. Nayak, K. L. More, H. M. Meyer, M. D. Biegalski, J. V. Li, and M. C. Gupta, "Properties of ultrafast laser textured silicon for photovoltaics," *Sol. Energy Mater. Sol. Cells* **95**(10), 2745–2751 (2011).
22. X. Feng and X. Wang, "Effects of laser fluence on near-field surface nanostructuring," *Appl. Surf. Sci.* **254**(13), 4201–4210 (2008).
23. M. Q. Jiang, Y. P. Wei, G. Wilde, and L. H. Dai, "Explosive boiling of a metallic glass superheated by nanosecond pulse laser ablation," *Appl. Phys. Lett.* **106**(2), 021904 (2015).
24. L. J. Zhao, M. G. Cheng, X. D. Yuan, and H. Wang, "Formation mechanism of a smooth, defect-free surface of fused-silica optics using rapid CO₂ laser polishing," *Int. J. Extrem. Manuf.* **1**(3), 035001 (2019).
25. J. S. Wang and P. J. Liew, "Repair of ultrasonic machining induced surface/subsurface cracks by laser irradiation," *Opt. Laser Technol.* **111**, 497–508 (2019).
26. O. Nebel, R. J. Arculus, T. J. Ivanic, R. Rapp, and K. J. A. Wills, "Upper Zone of the Archean Windimurra layered mafic intrusion, Western Australia: insights into fractional crystallisation in a large magma chamber," *J. Miner. Geochem.* **191**(1), 83–107 (2013).

27. J. Podleśny, "Effect of laser irradiation on the biochemical changes in seeds and the accumulation of dry matter in the faba bean," *Int. Agrophys.* **16**(3), e94274 (2002).
28. X. Yang, L. Hao, J. Chen, X. Cao, and Y. Wang, "Improved imaging quality of cluster LiDAR by optimizing laser energy distribution using an effective optical approach," *Opt. Commun.* **460**, 125181 (2020).
29. A. Hafiz, E. V. Bordatchev, and R. O. Tutunea-Fatan, "Experimental analysis of applicability of a picosecond laser for micro-polishing of micromilled Inconel 718 superalloy," *Int J Adv Manuf Technol* **70**(9-12), 1963–1978 (2014).
30. L. L. Taylor, J. Xu, M. Pomerantz, T. R. Smith, J. C. Lambropoulos, and J. Qiao, "Femtosecond Laser Polishing of Germanium towards Freeform Fabrication [Invited]," *Opt. Mater. Express* **9**(11), 4165–4177 (2019).
31. D. T. Attwood, D. W. Sweeney, J. M. Auerbach, and P. Lee, "Interferometric confirmation of radiation-pressure effects in laser-plasma interactions," *Phys. Rev. Lett.* **40**(3), 184–187 (1978).
32. W. W. Mullins and R. F. Sekerka, "Morphological Stability of a Particle Growing by Diffusion or Heat Flow," *J. Appl. Phys.* **34**(2), 323–329 (1963).
33. G. A. Giardini, V. Marotta, S. Orlando, and G. P. Parisi, "Photoexcitation in thin films deposited on silicon substrates by reactive pulsed laser ablation," *Int. J. Photoenergy* **3**(4), 213–216 (2007).
34. T. Meshram and J. W. Yan, "Generation of microcones on reaction-bonded silicon carbide by nanosecond pulsed laser irradiation," *Int J Adv Manuf Technol* **108**(4), 1039–1048 (2020).
35. L. L. Taylor, J. Qiao, and J. Qiao, "Optimization of femtosecond laser processing of silicon via numerical modeling," *Opt. Mater. Express* **6**(9), 2745–2758 (2016).